# PROCEEDINGS OF SPIE

SPIEDigitalLibrary.org/conference-proceedings-of-spie

# Emergent mechanical properties of biomimetic exoskeletal metamaterials

Ebrahimi, Hossein, Ali, Hessein, Stephen, Jeremy, Dharmavaram, Sanjay, Ghosh, Ranajay

Hossein Ebrahimi, Hessein Ali, Jeremy Stephen, Sanjay Dharmavaram, Ranajay Ghosh, "Emergent mechanical properties of biomimetic exoskeletal metamaterials," Proc. SPIE 11586, Bioinspiration, Biomimetics, and Bioreplication XI, 115860N (22 March 2021); doi: 10.1117/12.2584345



Event: SPIE Smart Structures + Nondestructive Evaluation, 2021, Online Only

# Emergent mechanical properties of biomimetic exoskeletal metamaterials

Hossein Ebrahimi<sup>a</sup>, Hessein Ali<sup>a</sup>, Jeremy Stephen<sup>b</sup>, Sanjay Dharmavaram<sup>c</sup>, and Ranajay Ghosh<sup>a</sup>

<sup>a</sup>Department of Mechanical and Aerospace Engineering, University of Central Florida, Orlando, FL, 32816, USA <sup>b</sup>Lockheed Martin, Orlando, FL <sup>c</sup>Department of Mathematics, Bucknell University, Lewisburg, PA, 17837, USA

#### ABSTRACT

Exoskeletons, such as scales on fishes and snakes were a critical evolutionary adaptation. Honed by millions of years of evolutionary pressures, they are inherently lightweight and yet multifunctional, aiding in protection, locomotion and optical camouflaging. This makes them an attractive candidate for biomimicry to produce high performance multifunctional materials with applications to soft robotics, wearables, energy efficient smart skins and on-demand tunable materials. Canonically speaking, biomimetic samples can be fabricating by partially embedding stiffer plate like segments on softer substrates to create a bi-material system, with overlapping scales. Recent investigations on their mechanics have shown that the origins of many of these behaviors are not merely due to load distribution but because of an intricate interplay of deformation, sliding and interfacial behavior. Such interplay give rise to property combinations that are typically not visible in the parent material of either the scales or the substrates. Here we review and present the origins of some of their fascinating behavior which include nonlinear and directional strain stiffening in both bending and twisting, dual nature of friction which combines both resistance as well as adding stiffness to motion, emergent viscosity in dynamic loading, and non-Hertzian contact mechanics. We will provide derivation of simple mathematical laws that govern structureproperty relationships that can help guide design. We will also demonstrate possibilities in non-mechanical properties such as elementary structural coloration and topography influenced mass deposition. We conclude by providing perspectives of future development and challenges.

Keywords: biomimetic, fish scale, exoskeleton, tailorable stiffness

## 1. INTRODUCTION

Exoskeleton elements such as fish scales were an early evolutionary innovation. <sup>1–4</sup> Appearing initially in fishes as scales for protection against predators and rivals, <sup>5,6</sup> their functions grew rapidly to aid locomotion, swimming, camouflage and thermal regulation. <sup>7–11</sup> It is therefore not surprising that the exoskeleton form not only survived evolutionary honing but thrived in the form of variegated scales, <sup>8,12,13</sup> furs, <sup>14,15</sup> papillae on feline tongues, <sup>16</sup> and scales on hairs. <sup>17,18</sup> Their mechanical advantages rest on not only their intricate material properties, <sup>19–21</sup> but also their orientation, overlap and distribution. This interplay between material and geometry lies at the heart of high performance of this structural system. Prior research investigating the mechanics of simple one-dimensional beams with embedded scales have shown the emergence of remarkable nonlinearity.

These nonlinearities are often emergent, i.e. not found in the individual parts but arise at the system level form mutual interactions of discrete but regularly arranged exoskeleton elements. Such periodic mutual reinforcement are also the hallmark of metamaterials, and like them the exoskeletal systems also exhibit unique

Further author information: (Send correspondence to R.G.)

 ${\it H.E.:}$ E-mail: ebrahimi@knights.ucf.edu

H.A.: E-mail: ashourh1@knights.ucf.edu

S.D.: E-mail: sd045@bucknell.edu

R.G.: E-mail: ranajay.ghosh@ucf.edu, Telephone: 1 407 823 3402

Bioinspiration, Biomimetics, and Bioreplication XI, edited by Akhlesh Lakhtakia, Mato Knez, Raúl J. Martín-Palma, Proc. of SPIE Vol. 11586, 115860N ⋅ © 2021 SPIE ⋅ CCC code: 0277-786X/21/\$21 ⋅ doi: 10.1117/12.2584345

property combinations. By harnessing such emergence, we can obtain hitherto unprecedented property ranges, combinations, tailorability and tunability in performance, not possible by mere mixing or traditional composite systems. These properties although not properly understood, were recognized by early humans. For instance, the features of scales were an inspiration for principles of armor design, <sup>5,12,22</sup> because overlapping scales can resist penetration and provide additional stiffness. <sup>5,12,23</sup> This inspiration is among the earliest interest in this area, which is based on the direct mimicry of the scaled integument for making scaled armors in the ancient times across the world. <sup>2,6,23–25</sup> Lamellar armors, fabricated out of lacing hard plates together, have been found in the ancient Egypt, <sup>2,24</sup> in the Scythian civilizations, <sup>24</sup> and in the Persian empire. <sup>23,24</sup> The scale armor also have been used by the Assyrian and Mongolian armed forces, <sup>23,24</sup> Roman troops, <sup>2,6</sup> and Japanese Samurai. <sup>6,25</sup> In spite of this early interest, little was known about the fundamental mechanics behind superior performance, which resulted in similar designs reappearing over years.

In addition to protection against external objects, which is mechanically an indentation type local deformation problem, global deformation modes such as bending and twisting of a substrate reveal equally interesting properties, for example a host of applications that require a structural mode of deformation such as soft robotics, prosthetics or morphing structures.<sup>26–29</sup> In a scale-covered structure, it is the role of scale engagements in modifying the global deformation behavior of the underlying structure. These include reversible nonlinear stiffening and locking behavior due to the sliding kinematics of the scales in one-dimensional substrates.<sup>30–36</sup>

1D substrates with stiff scales revealed strain stiffening due to sliding, scale deformation as well as friction in the bending mode of deformation.<sup>30</sup> Later simplification revealed the distinct nonlinear regimes of elasticity even without scale deformation or friction.<sup>33,35</sup> Nonlinearity due to frictional effects were further isolated and their effect on locking and dissipation quantified.<sup>34,36</sup> More studies revealed the limits of theoretical assumptions underpinning the models and their effect on predicted relationships.<sup>37–39</sup> Prior research has shown that bending and twisting of a substrate show small strain reversible nonlinear stiffening and locking behavior due to the sliding kinematics of the scales in one-dimensional substrates.<sup>30–39</sup> The universality of these behavior across bending of uniformly distributed scales, functionally graded scales and uniformly distributed twisting is an important discovery for these structures.

Fabrication methods for these scale-covered structures have been recently developed in 2D and 1D configuration. These fabricated structures show almost ten times more puncture resistance than soft elastomers. Generally, these scale-covered substrates can be fabricated in a number of ways. One strategy is using glue to attach stiff scales to deformable substrates. Here, the scales could be 3D printed stiff plates, <sup>33</sup>, <sup>35</sup>, <sup>38</sup>, <sup>40</sup> or steel sheets, <sup>39</sup> and the substrates could be made of Vinylpolysiloxane (VPS) elastomer, <sup>33</sup>, <sup>35</sup>, <sup>38</sup>, <sup>40</sup> or 3D printed flexible material, <sup>39</sup> with prefabricated grooves for scales embedding, as shown in Figure 1 (a). Other strategies comprise multi-material 3D printing with flexible and rigid material photopolymers associated to substrate and scales respectively, <sup>41</sup> a combination of laser engraving alumina strip for scales and stretch-and-release fabrication method, <sup>42</sup> and sewing cellulose acetate butyrate (CAB) scales on a polypropylene mesh using cotton thread. <sup>43</sup> For emulating intricate and naturally inspired structures, additive manufacturing can be regarded, <sup>44</sup> or a combination method of using female mold to arrange scales in a 2D overlapped arrangement, and casting silicone and then demolding can be utilized, <sup>45</sup> as shown in Figure 1 (b). In addition, 3D printed mold to cast silicone, <sup>46</sup> and multi-material 3D printing <sup>47</sup> have been used to mimic the scaled-like shark skin.



Figure 1. (a) Fabricated 1D scale-covered prototypes using glue the stiff scales into prefabricated grooves of deformable substrate. (b) Fabricated 2D scale-covered prototypes using female mold to arrange scales in a 2D overlapped arrangement.

Extending the dimensionality of the problem, two-dimensional substrates were also investigated. 31,32,43,48 These showed several similarities with their one-dimensional counterparts in bending. In this paper, we represent the emergent behavior scale-covered 1D structures under bending and twisting loads, including the frictional effects, then we investigate the mechanics of fish scale exoskeletal under combined loading in one-dimensional filamentous structure and two-dimensional plate with protruding scale-like features embedded on to the surface. Then, we investigate the puncture response of these structures. Finally, we conclude the emergent behaviors in the biomimetic exoskeletal metamaterials and discuss the future development and challenges in this area.

#### 2. BENDING OF SCALE-COVERED 1D BEAM

# 2.1 Mechanics of global bending deformation

To study the bending response of a scale-covered 1D beam, a beam with partially-embedded inclined stiff or rigid scales has been considered with the geometrical parameters shown in Figure 2 (a). By applying the bending load to the structure, the bent shape of the substrate can be envisaged as a circular arc of a beam, as shown in Figure 2 (a). A representative volume element (RVE) can be isolated by assuming the periodicity in scale engagements. To characterize the kinematics of this structure, the following nonlinear relationship have been established between the local angular deflection of the scales (scales' inclination angle)  $\theta$ , and the local substrate angular deflection  $\psi$ :<sup>33,34</sup>

$$\eta \psi \cos \psi / 2 - \sin(\theta + \psi / 2) = 0. \tag{1}$$

In Equation 1,  $\eta = l/d$  is called overlap ratio, where d and l are the scales spacing and the scales exposed length, respectively. <sup>33, 34</sup> Here, the curvature of the beam  $\kappa$  is defined as  $\kappa = \psi/d$ . By plotting this relationship for various  $\eta$ , a kinematic mechanisms map is obtained as shown in Figure 2 (b) for a particular case. This map shows the performance of the system under three kinematic regimes of operations including the "linear behavior" before the scale engagement (the horizontal part of each  $\eta$ 's curve), the "nonlinear stiffening" after the scale engagement (the ascending curved part of each  $\eta$ 's curve), and finally reach to a kinematically locked configuration, which the connection of these locked configurations for various  $\eta$ 's curve is formed the kinematic locking border (shown with black curve in Figure 2 (b)). The locking envelope obtained mathematically by satisfying  $\partial \psi/\partial \theta = 0$ . To find the moment–curvature response, the energy approach has been utilized. The applied work is  $W = L_B \int_0^{\kappa} M d\kappa$  where  $L_B$ , M, and  $\kappa$  are the substrate length, applied moment, and substrate curvature, respectively. The work is absorbed by the system as the beam strain energy  $\frac{1}{2}E_BIL_B\kappa^2$ , and scales—substrate joint rotation resistance  $\frac{1}{2}NK_B(\theta-\theta_0)^2$ , where  $E_BI$ ,  $N=L_B/d$ ,  $\theta_0$ , and  $K_B$  are the beam's bending rigidity, number of scales, initial inclination of scales, and scales torsional stiffness, respectively. <sup>33,34</sup> Finally, the moment–curvature response is derived by the energy—work balance on the beam as follows:

$$M(\kappa) = E_B I \kappa + K_B (\theta - \theta_0) \frac{\partial \theta}{\partial \psi} H(\kappa - \kappa_e). \tag{2}$$

Here,  $\kappa_e$  and  $H(\kappa - \kappa_e)$  are the engagement curvature and Heaviside step function, respectively. The Heaviside step function distinguishes the scales engagement by adding the nonlinear stiffening term  $K_B(\theta - \theta_0) \frac{\partial \theta}{\partial \psi}$ , just after the scales engagement to the moment response. Figure 2 (c) displays the moment response of the structure for a particular case with varying overlap ratio  $\eta$ . The developed model showed good agreements with finite element (FE) simulations for both kinematic and mechanic plot shown in Figure 2 (b) and (c).

#### 2.2 Frictional effects in bending

The effect of friction can be quantified in bending by considering force balance on the RVE assuming  $f_{\rm fr} = \mu N$  where  $f_{\rm fr}$ , N, and  $\mu > 0$  are the friction force, normal force, and coefficient of friction, respectively as shown in Figure 2 (a). This force balance leads to highly nonlinear relationship for the frictional force dependence on the nondimensionalized curvature  $\kappa/\kappa_e$ ,<sup>34</sup> as shown in Figure 2 (d) for a particular case with varying coefficient of friction  $\mu$ . Clearly, there is a sharp rise in friction forces for each  $\mu$  and the frictional force is singular at a certain curvature, which indicates configuration of "frictional locking" where the system behaves rigid at this point because the friction force between scales approaches to the infinite value. The friction locking is occurring

earlier than the kinematic, leads to advance locking envelope with increasing  $\mu$ , as shown in Figure 2 (e). In addition to the role of friction in the kinematic characteristics of the system by advancing the locking, the frictional dissipation work is involved in the energy—work balance of the system leads to extending the energy balance mentioned in Equation (2) to the following form:

$$M(\kappa) = E_B I \kappa + \left( K_B (\theta - \theta_0) \frac{\partial \theta}{\partial \psi} + f_{\rm fr} \frac{\mathrm{d}r}{\mathrm{d}\psi} \right) H(\kappa - \kappa_e). \tag{3}$$

Here, dr is the relative differential displacement of the friction force in the direction of sliding, which is discussed thoroughly in.<sup>34</sup> By adding the frictional dissipation work to the energy—work balance, the friction will have additional nonlinear stiffening effect after scales engagement as shown in the Figure 2 (f), as the post-engagement moment–curvature for a particular case with varying friction coefficients.

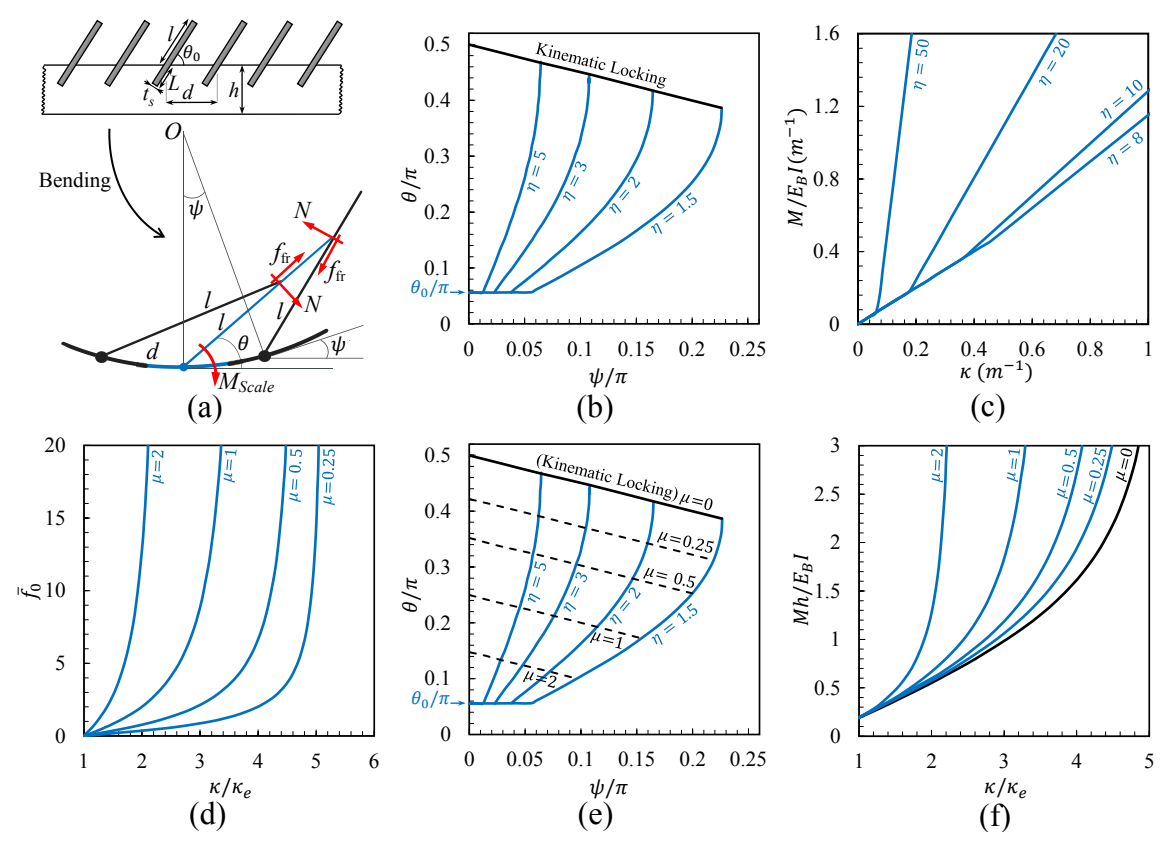


Figure 2. (a) The isolated RVE and free body diagram for bending load. (b) The kinematic mechanisms map. (c) The moment–curvature response. (d) nondimensionalized friction force vs curvature for various friction coefficients. (e) The kinematic mechanisms map with frictional effects. (f) The post-engagement moment–curvature for various friction coefficients.

# 3. TWISTING OF SCALE-COVERED 1D BEAM

# 3.1 Mechanics of global twisting deformation

In contrast to bending, the case of twisting is somewhat more complex because of the out of plane deformation. Early studies on the torsional response of the 2D scaled system seemed to indicate no significant stiffening like the bending,<sup>31</sup> because they considered the scales arrangement as parallel to the torsion axis, which leads to excessive torsion for scales engagement.<sup>35</sup> Thus, in a recent work we focused on oblique scales with oblique angle  $\alpha$  (in addition to inclination angle  $\theta$ ) under twisting load,<sup>35</sup> as shown in the RVE in Figure 3 (a). Here,

in addition to the overlap ratio  $\eta = l/d$ , we define additional dimensionless geometrical parameters including the dimensionless scale width  $\beta = b/d$ , and dimensionless substrate thickness  $\lambda = t/d$ , where b and t are the half width of scale, and half thickness of substrate, respectively. The following nonlinear relationship is obtained between the scales' inclination angle  $\theta$ , and the substrate's local twist angle  $\varphi$  using periodicity assumption on the twisting deformation:<sup>35,36</sup>

$$(\cos \varphi - 1) \Big( \beta \sin 2\alpha \sin \theta + \eta \cos^2 \alpha \sin 2\theta + 2\lambda \cos 2\alpha \cos \theta \Big) - 2 \cos \alpha \cos \varphi \sin \theta + 2 \sin \alpha \sin \varphi (\eta + \lambda \sin \theta) + 2 \cos \alpha \sin \varphi \cos \theta (\beta - \sin \alpha) = 0.$$

$$(4)$$

Here, the twisting curvature of the beam is called twist rate  $\Phi$ , which is defined as  $\Phi = \varphi/d$ . By plotting this relationship for various  $\eta$ , a kinematic mechanisms map is obtained as shown in Figure 3 (b) for a particular case, similar to bending case. Clearly, here again three distinct regimes of operation emerged including linear, nonlinear and kinematic locking. Using energy balance approach, similar to the bending, a nonlinear torque—twist rate relationship is derived:<sup>35</sup>

$$T(\Phi) = C_f C_w G_B I \Phi + K_\theta (\theta - \theta_0) \frac{\partial \theta}{\partial \varphi} H(\Phi - \Phi_e). \tag{5}$$

Here,  $C_w$  is the warping coefficient for non-circular cross section under twisting,<sup>49</sup> and  $C_f$  is the inclusion correction factor which accounts for the additional appreciable stiffness gain due to embedded parts of the rigid scales into deformable substrate.<sup>35,36</sup>

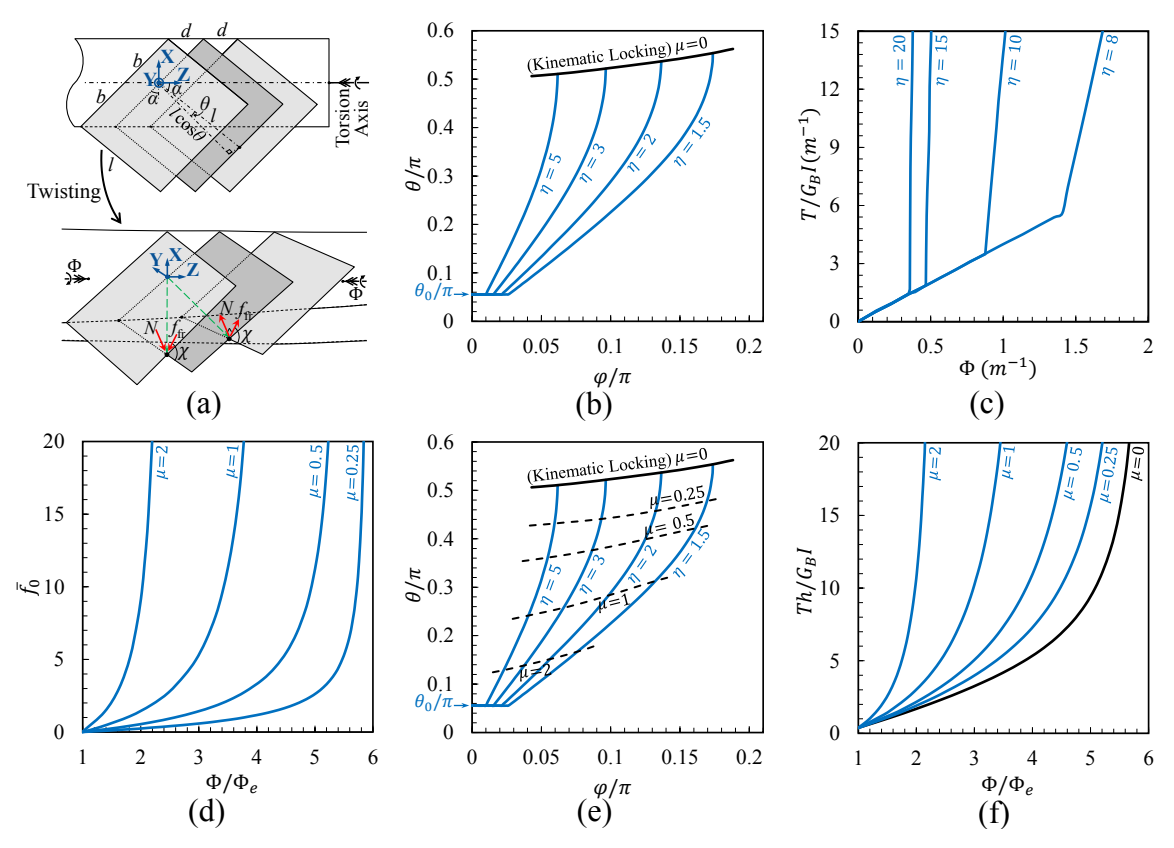


Figure 3. (a) The isolated RVE and free body diagram for twisting load. (b) The kinematic mechanisms map. (c) The torque—twist rate response. (d) non-dimensionalized friction force vs twist rate for various friction coefficients. (e) The kinematic mechanisms map with frictional effects. (f) The post-engagement torque—twist rate for various friction coefficients.

Also in this relationship,  $K_{\theta}$ ,  $\Phi_{e}$ , and  $H(\Phi - \Phi_{e})$  are the rotational spring constant for change in inclination angle  $\theta$ , engagement curvature, and Heaviside step function to track the scales engagement, respectively. This relationship creates the plot shown in Figure 3 (c), as the torque–twist rate response of the structure for a particular case with varying overlap ratio  $\eta$ , which shows a nonlinear stiffening after scales engagement same as the bending case.

# 3.2 Frictional effects in twisting

To study the effect of friction in twisting, similar method to the bending case is considered for the RVE force balance with the friction force  $f_{\rm fr}$ , and the normal force N represented in Figure 3 (a). This leads to an expression for the frictional force as discussed in detail in a recent work.<sup>36</sup> From this expression, a highly nonlinear plot is obtained for different coefficient of friction  $\mu$ , which displays the dependence of nondimensionalized friction force  $\bar{f}_0$  and nondimensionalized twist rate  $\Phi/\Phi_e$ , as shown in Figure 3 (d) for a particular case. The singularity in the friction force curves for each  $\mu$  indicates the frictional locking configuration same as bending case. Figure 3 (e) shows that the frictional locking happens earlier than kinematic locking with increasing the coefficient of friction  $\mu$ , leads to advance the locking envelope. By developing the energy—work balance of the system, an extended form is obtained for the equation (5) as followed:

$$T(\Phi) = C_f C_w G_B I \Phi + \left( K_\theta (\theta - \theta_0) \frac{\partial \theta}{\partial \varphi} + f_{fr} \frac{\mathrm{d}r}{\mathrm{d}\varphi} \right) H(\Phi - \Phi_e). \tag{6}$$

The value and direction of the relative differential displacement dr has been discussed in a recent work.<sup>36</sup> The additional term  $f_{\rm fr} \frac{dr}{d\varphi}$  is involving the frictional dissipation work to the energy–work balance of system. This leads to the additional nonlinear stiffening effect to the post-engagement torque–twist rate, which is shown for a particular case with varying friction coefficients in Figure 3 (f).

#### 4. COMBINED LOADS IN SCALE-COVERED 1D BEAM

The case of combined bending and twisting loads is much more challenging due to the mathematical complexity introduced by the three-dimensional nature of contact between scales. It is further compounded by their various possible modes of contact, as we shall see in this section. The kinematics of contact for this general case can be captured by strain variables  $\kappa_1$  and  $\kappa_2$ , which denote the bending curvature strains about the X-axis and Y-axis, and  $\kappa_3$ , the torsional strain due to the twist about the Z-axis. In this notation, for the cases discussed in Section 2 and 3, we have  $\kappa = \kappa_1$  and  $\Phi = \kappa_3$ , respectively. For prescribed and constant (bending and torsional) strains, the beam configuration is shown in Figure 4 (a). Scales engage for specific values of  $\theta$  that depend on the bending and torsional strains. Unlike the cases of pure bending and pure twisting as discussed in Section 2 and 3, the mathematical complexity inherent in the general case precludes a relatively straightforward algebraic relationship between  $\theta$  and the strain measures (akin to Equation (1) and (4)). Nevertheless, the dependence can be computed using the following steps:

- 1. We relate the beam's strains  $(\kappa_1, \kappa_1, \kappa_1)$  to the rotation of the scales via a rotation matrix.
- 2. We use the rotation matrix to map the equations of the two planes (containing the scales) back to their undeformed orientations.
- 3. Next, we compute the planes' intersection point(s). Due to the pull-back operation of step 2, the points' coordinates are in the reference configuration of the scales.
- 4. We determine if an intersection point falls within the (finite) scale's confines.
- 5. We rule out configurations that correspond to interpenetrating scales.

Using this procedure, we obtain Figure 4 (b), where we plot  $\theta$  at contact as a function of  $\kappa_3$  (for  $\kappa_1 = 0.2$ ,  $\kappa_2 = 0$ ,  $\eta = 3$ ,  $\beta = 1.25$ , and  $\alpha = 30^{\circ}$ ). We observe four distinct modes of contact which are color coded in the figure as follows:

- a) Black: Left edge of the first scale makes contact with top edge of the second. Configuration is shown as scheme A in Figure 4 (b).
- b) Red: Corner of the first scale makes contact with face/edge of the second scale. Configurations are shown as the scheme B, and C in Figure 4 (b).

- c) Green: Right edge of the first scale makes contact with top edge of the second. Configurations are shown as the scheme D and E in Figure 4 (b).
- d) Blue: Top edges of the first and second scales make contact. Configurations are shown as the scheme F and G in Figure 4 (b).

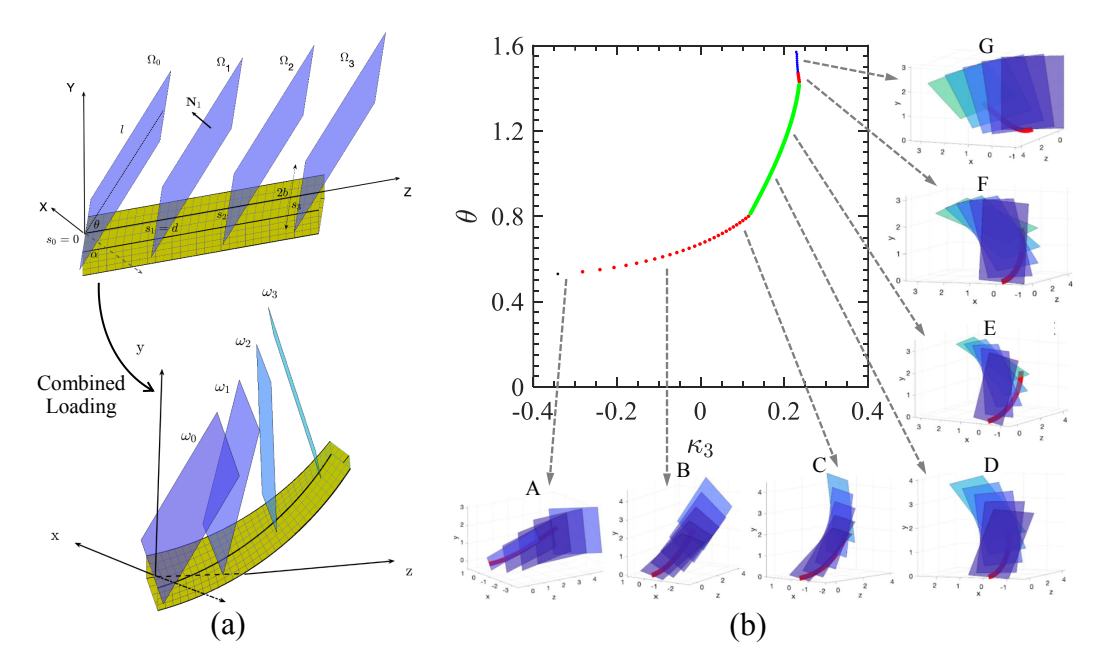


Figure 4. (a) Schematics showing the substrate beam with rectangular scales in the undeformed and deformed configurations under combined loading. (b)  $\kappa_3$  vs  $\theta$  for different values of  $\kappa_1 = 0.2$  showing various contacts. Here  $\kappa_2 = 0$ ,  $\eta = 3$ ,  $\beta = 1.25$ , and  $\alpha = 30$ .

Note that the change in slopes as the modes of contact changes. This feature manifests as a discontinuity in the moment-strain relationship, a novel emergent behavior not observed in our earlier works. 33–36

In Figure 5 (a), we plot scales' inclination angle  $\theta$  as a function of  $\kappa_3$  for various values of bending strains,  $\kappa_1$ . We note from the figure that depending on  $\kappa_1$ , different modes of engagement dominate the behavior of the system. Observe that scales lock at the same angle  $\theta \approx 1.47$ , irrespective of  $\kappa_1$ . For small non-zero  $\kappa_1$ , the slope discontinuity in the curves as we transition from red to green curves suggests a sudden stiffening behavior of the system. This feature seems to vanish at larger  $\kappa_1$  values.

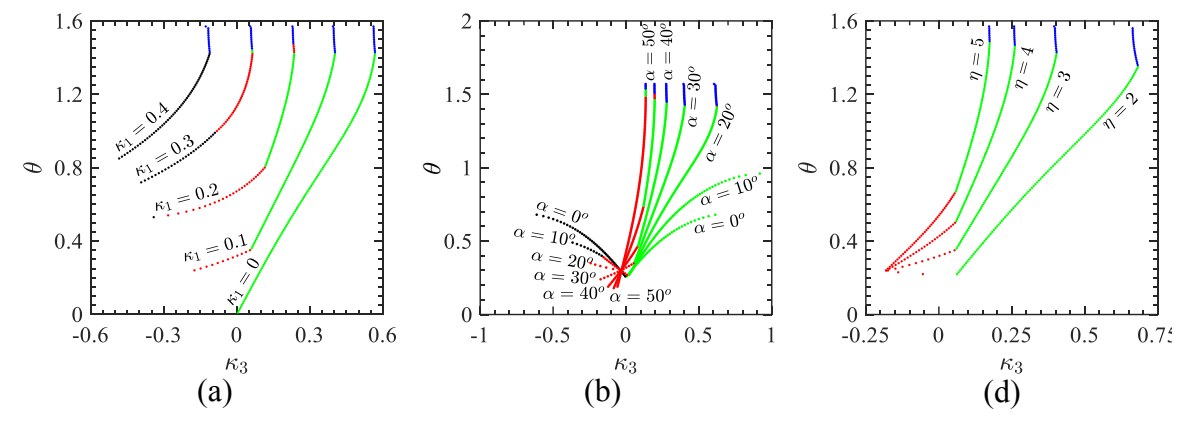


Figure 5. (a)  $\theta$  vs  $\kappa_3$  for different values of  $\kappa_1$ . Here  $\eta = 3$ ,  $\beta = 1.25$ , and  $\alpha = 30^{\circ}$ . (b)  $\theta$  vs  $\kappa_3$  for different values of  $\alpha$ . Here  $\eta = 3$ ,  $\beta = 1.25$ , and  $\kappa_1 = 0.1$ . (c)  $\theta$  vs  $\kappa_3$  for different values of  $\eta$ . Here  $\kappa_1 = 0.15$ ,  $\beta = 1.25$ , and  $\alpha = 30^{\circ}$ .

In Figure 5 (b), we plot  $\theta$  vs  $\kappa_3$  for different values of  $\alpha$  (for  $\eta = 3$ ,  $\beta = 1.25$ , and  $\kappa_1 = 0.1$ ). We observe that for small values of  $\alpha$ , there is a stiffening behavior as  $\kappa_3 \approx 0$  is either increased or decreased, with a minimum stiffness at  $\kappa_3 = 0$ . This behavior disappears for larger  $\alpha$  as can be inferred from the monotonic curves in the figure for these values. We also observe that locking angle  $\theta_{lock}$  is influenced by  $\alpha$  with no locking below a critical  $\alpha$ . In Figure 5 (c), we plot  $\theta$  vs  $\kappa_3$  for different values of  $\eta$  (for  $\kappa_1 = 0.15$ ,  $\beta = 1.25$ , and  $\alpha = 30^{\circ}$ ). We see here again that  $\eta$  influences the angle of locking, which is similar to our earlier findings for pure bending and twisting.

#### 5. MECHANICS OF SCALE-COVERED 2D PLATE

In this section we consider a deformable plate with scales covering its surface. The scales are partially embedded on the top surface of the plate with staggered arrangement as shown in Figure 6 (a). We consider the deformable plate as a square shape  $(W_{sub} = L_{sub})$  with thickness 2t. The exposed length of scales and the width of them are l and 2b, respectively. The longitudinal and transverse distance between the scales are d and c. Therefore, in addition to previous dimensionless parameters  $\eta = l/d$ ,  $\beta = b/d$ , and  $\lambda = t/d$ , we will define  $\delta = c/d$ , as the dimensionless clearance between the scales. According to classical plate theory or the Kirchhoff plate theory, <sup>50</sup> the moment–curvature response of two in-plane directions (here Z and X direction) are as follows:

$$M_z(\kappa_z, \kappa_x) = \frac{E_B I}{1 - \nu^2} (\kappa_z + \nu \kappa_x),$$

$$M_x(\kappa_x, \kappa_z) = \frac{E_B I}{1 - \nu^2} (\kappa_x + \nu \kappa_z).$$
(7)

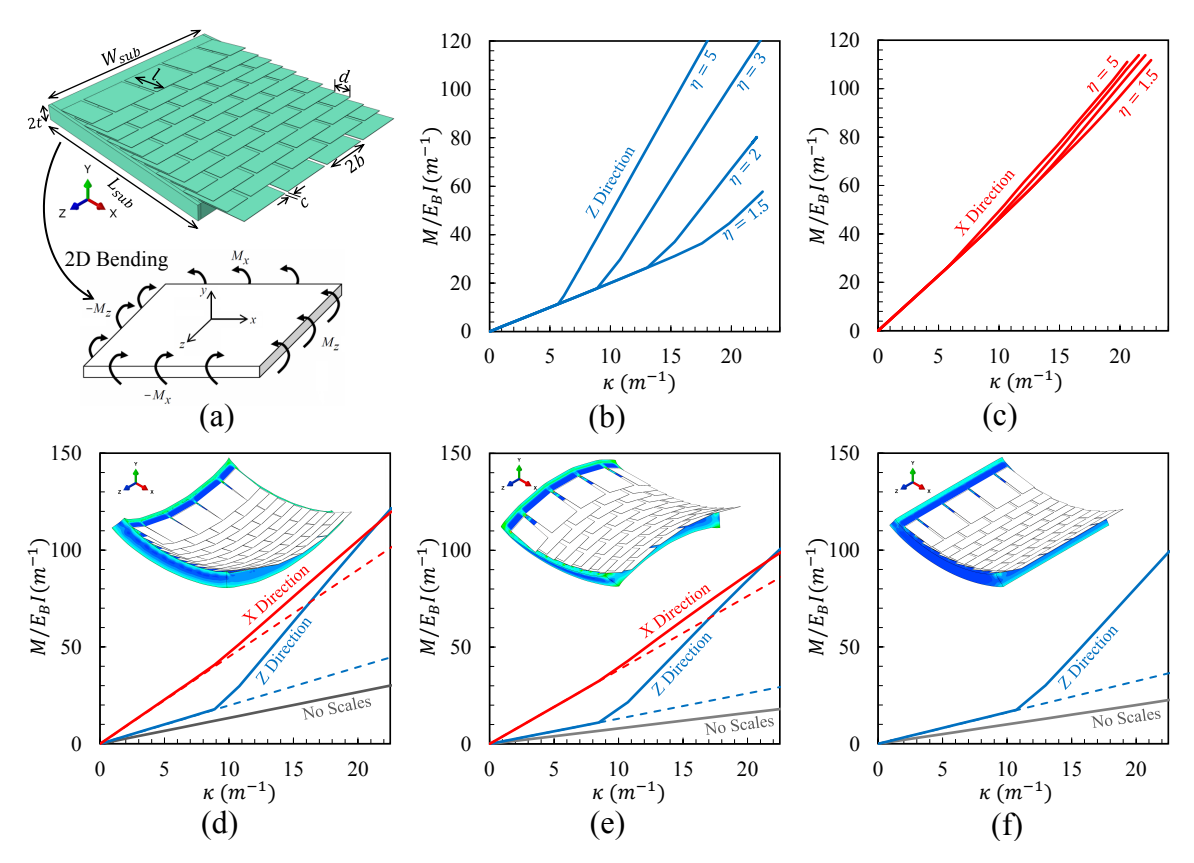


Figure 6. (a) The geometry and two directional bending loads of scale-covered plate. (b) The moment–curvature response for various  $\eta$  in Z direction. (c) The moment–curvature response for various  $\eta$  in X direction. (d) The moment–curvature response for first load case  $(M_z > 0)$  and  $M_x > 0$ . (e) The moment–curvature response for second load case  $(M_z > 0)$  and  $M_x < 0$ . (f) The moment–curvature response for third load case  $(M_z > 0)$  and  $M_x < 0$ .

Similar to the pure bending and pure twisting case, adding the rigid scales to the surface of the plate with provide additional stiffness response after scales engagement which can be modeled as rotational springs, here for two different in-plane direction as  $K_{\theta,z}$  and  $K_{\theta,x}$ . Also, here we have the inclusion effect as the additional appreciable stiffness gain due to the scales inclusion into the substrate similar to the twisting case.<sup>35,36</sup> This effect will model as the inclusion correction factors for two in-plane directions  $C_{f,z}$  and  $C_{f,z}$ . According to these considerations, the moment–curvature response of scale-covered 2D plate for two in-plane directions will model as follows:

$$M_{z}(\kappa_{z}, \kappa_{x}) = \frac{C_{f,z}E_{B}I}{1 - \nu^{2}}(\kappa_{z} + \nu\kappa_{x}) + \frac{K_{\theta,z}}{d}(\theta - \theta_{0})\frac{\partial\theta}{\partial\kappa_{z}}H(\kappa_{z} - \kappa_{z,e}),$$

$$M_{x}(\kappa_{x}, \kappa_{z}) = \frac{C_{f,x}E_{B}I}{1 - \nu^{2}}(\kappa_{x} + \nu\kappa_{z}) + \frac{K_{\theta,x}}{d}(\theta - \theta_{0})\frac{\partial\theta}{\partial\kappa_{x}}H(\kappa_{x} - \kappa_{x,e}).$$
(8)

In Figure 6 (b) and (c), the moment–curvature responses are displayed for a particular case with various  $\eta$  in Z and X directions, which is obtained from finite element analyses. The emergent stiffness gain after scales engagement is clearly observed which is dependence on  $\eta$  value, and this stiffness gain has higher effect in Z direction moment. In this first load case the applied moments in both in-plane directions are positive ( $M_z > 0$  and  $M_x > 0$ ). In Figure 6 (d), the moment–curvature response of the first load case has been compared with the response of counterpart plane plate without scales. Clearly, the stiffness gains due to the inclusions (dashed curves) and emergent stiffness due to scales engagement can be observed. Figure 6 (e) and (f) display the moment–curvature response of the second load case ( $M_z > 0$  and  $M_x < 0$ ), and the third load case ( $M_z > 0$  and  $M_x = 0$ ). In these plots similar to the first load case, inclusion effect and scales engagement have been observed. The results shown in Figure 6 (b)-(f) are obtained from finite element simulations, and only the results of plain plate have been compared with theoretical results from Equation (7), which shown a great agreements.

# 6. NON-PENETRATIVE CONTACT RESPONSE

As described earlier, some of the earliest uses of scaly substrates have been for armor protection. However, non-penetrative contact typically possible in the robotic gripping applications are equally fascinating. One way to highlight the interplay of scales and indenter, is by carrying out indentation experiments with different indenter nose radius, representing various types of contacts ranging from the very sharp to blunt. As seen in Figure 7, a sharp indenter can induce an anisotropic contact area, which is mitigated as the indenter radius increases. The origin of the anisotropy is due to the arrangement and orientation of the scales. A sharp indenter induces preferential engagement of scales on one side (right in the figure) compared to other. This breaks the symmetry of the contact area.<sup>51</sup>

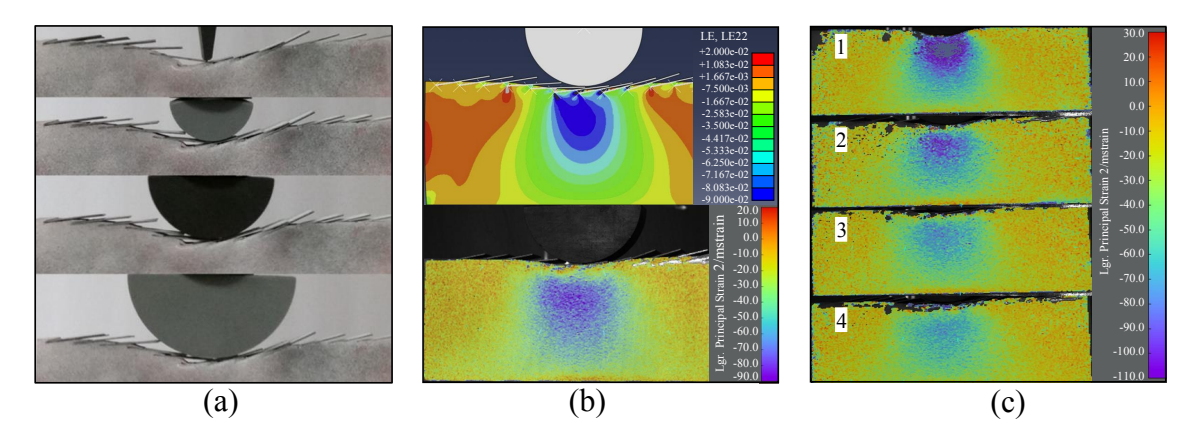


Figure 7. (a) Decrease in loading surface anisotropy with increasing indenter radius, where R=2.5, 25, 37.5, and 50 mm. (b) Strain concentration, and propagation from embedded scale tips, displayed in finite element and DIC analyses. (c) Plain,  $\eta=1.2$ ,  $\eta=1.6$ , and  $\eta=2.4$  samples shown under equal loading of 80 N show reduced strain concentrations with increasing  $\eta$ .

It is observed that as the indenter radius increases, for a given scale length, the anisotropy in the contact surface decreases. This is due to the ability of larger indenters to come into contact with additional scales to the left as the substrate deforms. From this, it is anticipated that larger indenters, capable of contacting multiple scales at the onset, could become significant in the force-displacement response. This requires further study.

We compare our FE simulations experimentally with full field 3D Digital Image Correlation (DIC) measurements. The 3D DIC analyses were run to confirm the finite element simulation results for the experimental configurations, where R=37.5 mm and  $\eta=1.2$ , 1.6 and 2.4. The strains in the samples were observed to follow the same distribution, with the strain propagating from the embedded scale ends, as shown in Figure 7 (b). Additionally, it is shown that the addition of scales, with increasing  $\eta$ , increases the distribution and reduces strain concentration, as shown in Figure 7 (c), where the four experimental samples are shown under a load of 80 newtons.

#### 7. EMERGENT DYNAMIC BEHAVIOR OF SCALE-COVERED 1D BEAM

In this section, we provide an emergent dynamical behavior that arises due to the free oscillation of scale-covered 1D beams. The equation of motion of such beams can be obtained using the variational energy equation that is derived from Hamilton principle of least action  $\delta \int_{t_1}^{t_2} (\bar{T} - \bar{V}) \mathrm{d}t = 0$ . In this formula,  $\bar{T}$  refers to the kinetic energy per unit length and  $\bar{V}$  denotes the strain energy per unit length of both substrate and scales. The resulting equation of motion can be written as  $m \frac{\partial^2 \bar{y}}{\partial \bar{x}^2} + \frac{\partial^2 M(\kappa)}{\partial \bar{x}^2} = 0$ , where m is the mass of scale-covered beam and  $M(\kappa)$  was presented earlier in Equation 3. Without loss of generality, we assume a simply supported beam and an initial velocity conditions that ensures the activation of only the first mode of vibration. We solve the equation of motion numerically using the direct numerical integration method called Newmark along with Newton-Raphson.

We plot the deflection of the middle point of the beam,  $\bar{y}$  normalized by the radius of gyration against the time which is also normalized by the undamped period of a plain beam,  $\bar{t}$  for the case of  $\eta=10$  and various coefficients of frictions,  $\mu$  as shown in Figure 8. The free oscillation response highlights that the most interesting feature of the simple structure is the exponential decay, Figure 8, that arises due to the interfacial friction between scales unlike the most common spring-mass system, which indicates a linear decay in the response due to dry friction.<sup>53</sup>

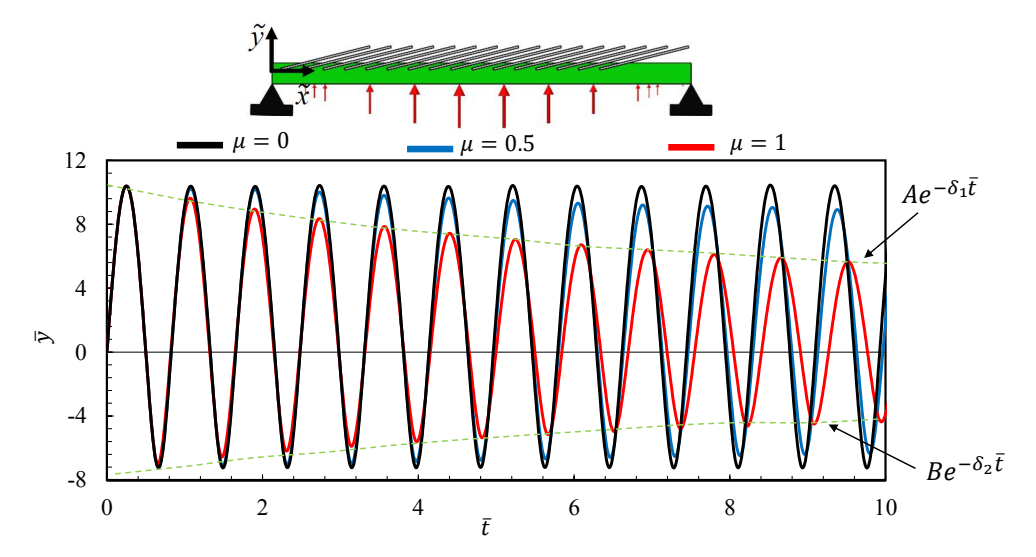


Figure 8. Free vibration of the midpoint of a simply supported biomimetic scale-covered beam with 25 scales,  $\theta_0 = 3^{\circ}$ ,  $\eta = 10$ , and various coefficients of frictions  $\mu$ . The deflection is normalized by vertical length scale (radius of gyration) and the time is normalized by the natural frequency and time period of the plain elastic substrate. The increase in the interfacial friction between neighboring scales leads an anisotropy in the exponential decay of both smooth and scaled side of the beam, illustrated by exponential decay  $\delta_1$  and  $\delta_2$ . Inset illustrates the case study tested.

The difference in response implies a geometric regime transformation of damping from dry friction to viscous drag. The revealed dampening phenomena, also called "viscous emergence", which resembles viscous dumping behavior of vibrating structures, was pronounced with postulation of only dry Coulomb friction. However, the similarities with viscously damped system is limited. For conventional damped oscillators, the decaying behavior continues forever until motion stops, but in this biomimetic system the decay will not lead to a complete stop of the system but rather until deflection is small enough that scales may not engage any more, returning the system to a conservative system (i.e., the slightly artificially damped system). Note that the increase in interfacial friction provides different stiffening mechanisms on each side of the beam due to the steady loss energy in each cycle. Thus, the topology-induced nonlinearity brought about the overlapping of scales provides a significant anisotropy of frictional behavior, giving rise to emergent behavior tailorability through interfacial and geometric parameters, here the control parameters can be the overlap ratio of scales  $\eta$  and the coefficient of friction between neighboring scales  $\mu$ .

# 8. MASS DEPOSITION ON TOPOGRAPHIC SURFACES

Surfaces of semi-aquatic mammals are highly vulnerable to biofilm growth, yet furry mammals that reside at the interface of water and sunlight practically escape this burden, despite the available provisions for microorganism proliferation. The complex but conspicuous scaly structures on the surface of the furs, as evidenced by scanning electron microscope images have long been hypothesized to be a very important factor mediating this behavior. Hence, surfaces with topographic features, like biomimetic scales, provide a promising avenue for antifouling strategies. In light of this, a simple model at quiescent flow is described which can shed some light on the role of deformation and topology. Here, a steady state model is constructed where the external fouling transport is assumed to be diffusive in nature. The steady-state diffusion is modeled by the Laplacian  $\nabla^2 C = 0$  in an infinite domain surrounding the fur. The fouling is assumed to be a general first order rate equation. This means the flux of mass deposited on the surface q is proportional to its concentration C, i.e., q = kC. Using these assumptions, the role of deformation and topology of a beam with scale-like topography on its surface can be seen in Figure 9. The plot illustrates the total mass aggregated per unit length along the surface against various configurations of deformation.

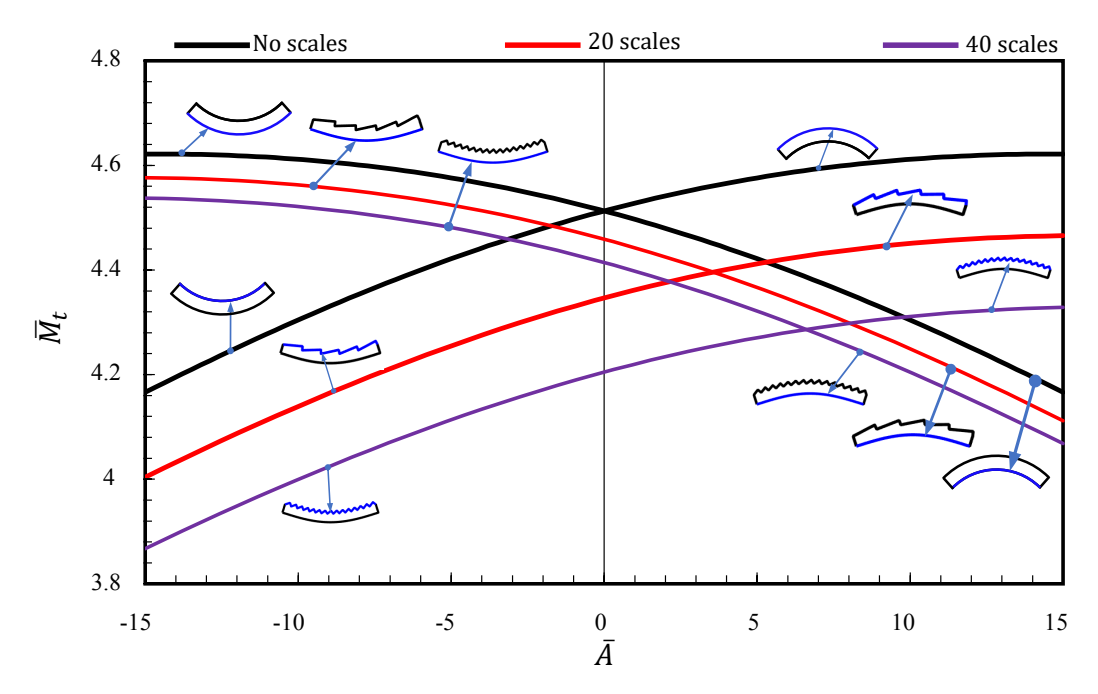


Figure 9. Mass deposition per unit length along the upper and lower surface of plain beam and scale-like topographic beam with various scales density surrounded by infinite media and the concentration at the far-filed is constant  $C_{\infty} = 10$  while k = 1. The cases presented include 20 and 40 scales arranged on the surface with an initial angle of 5°.

Here it is assumed that the beam deforms in a sinusoidal shape, where the amplitude of the shape function of the beam is normalized by the thickness  $\bar{A}$  and varied from convex to concave. The total mass is expressed as  $M_t = \frac{1}{L_S} \int_{L_S} q \mathrm{d}s$ , where ds is a line element length of either the topographic or smooth surface,  $L_s$  refers to the total arc length of the surface, and q represents the flux of deposited mass. The figure evidently ensures that mass deposition per unit length can be significantly reduced on the upper surface of convex configuration. In particular, we notice that density of topography (i.e., more scales added to the surface) also leads to less deposition when presented along the the upper surface of convex configuration and the opposite is true for concave configurations. Interestingly, the imposition of topography on only one surface provides anisotropy in the amount of deposited mass as compared to smooth surfaces on both sides of the beam. In summary, topography and deformation provide an imperative bearing on mass deposition or biofouling of surfaces, giving rise to antifouling surface design tailorability through topographic surfaces and deformation.

## 9. CONCLUSION

we have demonstrated a new paradigm of designing bioinspired tailorable/tunable structures – leveraging the phenomena of emergence to generate remarkable properties. And most importantly, these properties can be accessed systematically from building blocks and specific emergent processes can be activated, leading to a new class of smart structures. These synthetic materials can provide tailorable mechanical and physical response in different loading and material conditions. This outstanding feature could be useful in different applications including soft robotic, camouflage, substrate design, deployable structures, protective wearables, etc.

#### ACKNOWLEDGMENTS

This work was supported by the United States National Science Foundation's Civil, Mechanical, and Manufacturing Innovation, CAREER Award #1943886.

#### REFERENCES

- [1] Onozato, H. and Watabe, N., "Studies on fish scale formation and resorption," Cell and tissue research 201(3), 409–422 (1979).
- [2] Chen, I. H., Kiang, J. H., Correa, V., Lopez, M. I., Chen, P.-Y., McKittrick, J., and Meyers, M. A., "Armadillo armor: mechanical testing and micro-structural evaluation," *Journal of the mechanical behavior of biomedical materials* 4(5), 713–722 (2011).
- [3] Di-Poï, N. and Milinkovitch, M. C., "The anatomical placode in reptile scale morphogenesis indicates shared ancestry among skin appendages in amniotes," *Science Advances* **2**(6), e1600708 (2016).
- [4] Chang, C., Wu, P., Baker, R. E., Maini, P. K., Alibardi, L., and Chuong, C.-M., "Reptile scale paradigm: Evo-devo, pattern formation and regeneration," The International journal of developmental biology 53(5-6), 813 (2009).
- [5] Yang, W., Chen, I. H., Gludovatz, B., Zimmermann, E. A., Ritchie, R. O., and Meyers, M. A., "Natural flexible dermal armor," *Advanced Materials* **25**(1), 31–48 (2013).
- [6] White, Z. W. and Vernerey, F. J., "Armours for soft bodies: how far can bioinspiration take us?," *Bioinspiration & biomimetics* **13**(4), 041004 (2018).
- [7] Naleway, S. E., Taylor, J. R., Porter, M. M., Meyers, M. A., and McKittrick, J., "Structure and mechanical properties of selected protective systems in marine organisms," *Materials Science and Engineering: C* 59, 1143–1167 (2016).
- [8] Prum, R. O., Quinn, T., and Torres, R. H., "Anatomically diverse butterfly scales all produce structural colours by coherent scattering," *Journal of Experimental Biology* **209**(4), 748–765 (2006).
- [9] Colbert, E. H. et al., "Evolution of the vertebrates. a history of the backboned animals through time.," Evolution of the vertebrates. A history of the backboned animals through time. (1955).
- [10] Arciszewski, T. and Cornell, J., "Bio-inspiration: Learning creative design principia," in [Workshop of the European Group for Intelligent Computing in Engineering], 32–53, Springer (2006).
- [11] Huang, J., Wang, X., and Wang, Z. L., "Controlled replication of butterfly wings for achieving tunable photonic properties," *Nano letters* **6**(10), 2325–2331 (2006).

- [12] Wang, B., Yang, W., Sherman, V. R., and Meyers, M. A., "Pangolin armor: overlapping, structure, and mechanical properties of the keratinous scales," *Acta biomaterialia* 41, 60–74 (2016).
- [13] Greene, H. W., [Snakes: the evolution of mystery in nature], Univ of California Press (1997).
- [14] Meyer, W., Schnapper, A., and Hülmann, G., "The hair cuticle of mammals and its relationship to functions of the hair coat," *Journal of Zoology* **256**(4), 489–494 (2002).
- [15] Krsmanovic, M., Biswas, D., Ali, H., Kumar, A., Ghosh, R., and Dickerson, A. K., "Hydrodynamics and surface properties influence biofilm proliferation," *Advances in Colloid and Interface Science*, 102336 (2020).
- [16] Noel, A. C. and Hu, D. L., "The tongue as a gripper," Journal of Experimental Biology 221(7), jeb176289 (2018).
- [17] Garcia, M. L., Epps, J. A., Yare, R. S., and Hunter, L. D., "Normal cuticle-wear patterns in human hair," J Soc Cosmet Chem 29(3), 155 (1978).
- [18] Yu, Y., Yang, W., Wang, B., and Meyers, M. A., "Structure and mechanical behavior of human hair," *Materials Science and Engineering: C* 73, 152–163 (2017).
- [19] Zhu, D., Barthelat, F., and Vernereyb, F., "Intricate multiscale mechanical behaviors of natural fish-scale composites," *Handbook of Micromechanics and Nanomechanics ed S. Li and X. Gao* (2013).
- [20] Song, J., Ortiz, C., and Boyce, M. C., "Threat-protection mechanics of an armored fish," *Journal of the mechanical behavior of biomedical materials* **4**(5), 699–712 (2011).
- [21] Zhu, D., Ortega, C. F., Motamedi, R., Szewciw, L., Vernerey, F., and Barthelat, F., "Structure and mechanical performance of a "modern" fish scale," *Advanced Engineering Materials* **14**(4), B185–B194 (2012).
- [22] Zimmermann, E. A., Gludovatz, B., Schaible, E., Dave, N. K., Yang, W., Meyers, M. A., and Ritchie, R. O., "Mechanical adaptability of the bouligand-type structure in natural dermal armour," *Nature communications* 4, 2634 (2013).
- [23] Ehrlich, H., "Materials design principles of fish scales and armor," in [Biological Materials of Marine Origin], 237–262, Springer (2015).
- [24] Dien, A. E., "A brief survey of defensive armor across asia," Journal of East Asian Archeology, 2–3 (2000).
- [25] Studart, A. R., "Biological and bioinspired composites with spatially tunable heterogeneous architectures," *Advanced Functional Materials* **23**(36), 4423–4436 (2013).
- [26] Sadati, S. H., Noh, Y., Naghibi, S. E., Althoefer, K., and Nanayakkara, T., "Stiffness control of soft robotic manipulator for minimally invasive surgery (mis) using scale jamming," in [Intelligent Robotics and Applications], 141–151, Springer (2015).
- [27] Wei, Y., Chen, Y., Ren, T., Chen, Q., Yan, C., Yang, Y., and Li, Y., "A novel, variable stiffness robotic gripper based on integrated soft actuating and particle jamming," Soft Robotics 3(3), 134–143 (2016).
- [28] Roche, E. T., Horvath, M. A., Wamala, I., Alazmani, A., Song, S.-E., Whyte, W., Machaidze, Z., Payne, C. J., Weaver, J. C., Fishbein, G., et al., "Soft robotic sleeve supports heart function," *Science Translational Medicine* 9(373), eaaf3925 (2017).
- [29] Ali, H., Ebrahimi, H., Stephen, J., Warren, P., and Ghosh, R., "Tailorable stiffness lightweight soft robotic materials with architectured exoskeleton," in [AIAA Scitech 2020 Forum], 1551 (2020).
- [30] Vernerey, F. J. and Barthelat, F., "On the mechanics of fishscale structures," *International Journal of Solids and Structures* **47**(17), 2268–2275 (2010).
- [31] Vernerey, F. J., Musiket, K., and Barthelat, F., "Mechanics of fish skin: A computational approach for bio-inspired flexible composites," *International Journal of Solids and Structures* **51**(1), 274–283 (2014).
- [32] Vernerey, F. J. and Barthelat, F., "Skin and scales of teleost fish: Simple structure but high performance and multiple functions," *Journal of the Mechanics and Physics of Solids* **68**, 66–76 (2014).
- [33] Ghosh, R., Ebrahimi, H., and Vaziri, A., "Contact kinematics of biomimetic scales," *Applied Physics Letters* **105**(23), 233701 (2014).
- [34] Ghosh, R., Ebrahimi, H., and Vaziri, A., "Frictional effects in biomimetic scales engagement," *EPL (Euro-physics Letters)* **113**(3), 34003 (2016).
- [35] Ebrahimi, H., Ali, H., Horton, R. A., Galvez, J., Gordon, A. P., and Ghosh, R., "Tailorable twisting of biomimetic scale-covered substrate," *EPL (Europhysics Letters)* **127**(2), 24002 (2019).
- [36] Ebrahimi, H., Ali, H., and Ghosh, R., "Coulomb friction in twisting of biomimetic scale-covered substrate," *Bioinspiration & Biomimetics* **15**(5), 056013 (2020).

- [37] Ghosh, R., Ebrahimi, H., and Vaziri, A., "Non-ideal effects in bending response of soft substrates covered with biomimetic scales," *Journal of the mechanical behavior of biomedical materials* **72**, 1–5 (2017).
- [38] Ali, H., Ebrahimi, H., and Ghosh, R., "Bending of biomimetic scale covered beams under discrete non-periodic engagement," *International Journal of Solids and Structures* **166**, 22–31 (2019).
- [39] Ali, H., Ebrahimi, H., and Ghosh, R., "Tailorable elasticity of cantilever using spatio-angular functionally graded biomimetic scales," *Mechanics of Soft Materials* 1, 10 (2019).
- [40] Ali, H., Ebrahimi, H., and Ghosh, R., "Frictional damping from biomimetic scales," *Scientific Reports* **9**(1), 14628 (2019).
- [41] Connors, M., Yang, T., Hosny, A., Deng, Z., Yazdandoost, F., Massaadi, H., Eernisse, D., Mirzaeifar, R., Dean, M. N., Weaver, J. C., et al., "Bioinspired design of flexible armor based on chiton scales," *Nature communications* **10**(1), 1–13 (2019).
- [42] Martini, R. and Barthelat, F., "Stretch-and-release fabrication, testing and optimization of a flexible ceramic armor inspired from fish scales," *Bioinspiration & biomimetics* **11**(6), 066001 (2016).
- [43] Funk, N., Vera, M., Szewciw, L. J., Barthelat, F., Stoykovich, M. P., and Vernerey, F. J., "Bioinspired fabrication and characterization of a synthetic fish skin for the protection of soft materials," *ACS applied materials & interfaces* 7(10), 5972–5983 (2015).
- [44] Johnson, A., Bingham, G., and Majewski, C. E., "The design and assessment of bio-inspired additive manufactured stab-resistant armour," *Virtual and Physical Prototyping* **13**(2), 49–57 (2018).
- [45] White, Z., Shen, T., Volk, E. M., and Vernerey, F. J., "The role of surface properties on the penetration resistance of scaled skins," *Mechanics Research Communications* **98**, 1–8 (2019).
- [46] Yasuda, Y., Zhang, K., Sasaki, O., Tomita, M., Rival, D., and Galipon, J., "Manufacturing of biomimetic silicone rubber films for experimental fluid mechanics: 3d printed shark skin molds," *Journal of The Electrochemical Society* **166**(9), B3302 (2019).
- [47] Wen, L., Weaver, J. C., and Lauder, G. V., "Biomimetic shark skin: design, fabrication and hydrodynamic function," *Journal of Experimental Biology* **217**(10), 1656–1666 (2014).
- [48] Martini, R., Balit, Y., and Barthelat, F., "A comparative study of bio-inspired protective scales using 3d printing and mechanical testing," *Acta biomaterialia* **55**, 360–372 (2017).
- [49] Ugural, A. C. and Fenster, S. K., [Advanced mechanics of materials and applied elasticity], Pearson Education (2011).
- [50] Bauchau, O. A. and Craig, J. I., [Structural analysis: with applications to aerospace structures], vol. 163, Springer Science & Business Media (2009).
- [51] Stephen, J., "Contact mechanics of fish scale inspired exoskeletal components on a nonlinear elastic substrate," (2020).
- [52] Ahmadian Saieni, H., "Non-linear vibrations of tensegrity structures," (2012).
- [53] Meirovitch, L., [Fundamentals of vibrations], Waveland Press (2010).